Ultrastrong Coupling of the Cyclotron Transition of a 2D Electron Gas to a THz Metamaterial

G. Scalari, *et al.*

Science **335**, 1323 (2012);
DOI: 10.1126/science.1216022

Ultrastrong Coupling of the Cyclotron Transition of a 2D Electron Gas to a THz Metamaterial

G. Scalari,[1,*] C. Maissen,[1] D. Turčinková,[1] D. Hagenmüller,[2] S. De Liberato,[2] C. Ciuti,[2] C. Reichl,[3] D. Schuh,[4] W. Wegscheider,[3] M. Beck,[1] J. Faist[1]

Artificial cavity photon resonators with ultrastrong light-matter interactions are attracting interest both in semiconductor and superconducting systems because of the possibility of manipulating the cavity quantum electrodynamic ground state with controllable physical properties. We report here experiments showing ultrastrong light-matter coupling in a terahertz (THz) metamaterial where the cyclotron transition of a high-mobility two-dimensional electron gas (2DEG) is coupled to the photonic modes of an array of electronic split-ring resonators. We observe a normalized coupling ratio, $\frac{\Omega}{\omega_c} = 0.58$, between the vacuum Rabi frequency, Ω, and the cyclotron frequency, ω_c. Our system appears to be scalable in frequency and could be brought to the microwave spectral range with the potential of strongly controlling the magnetotransport properties of a high-mobility 2DEG.

Enhancement and tunability of light-matter interaction is crucial for fundamental studies of cavity quantum electrodynamics (QED) and for applications in classical and quantum devices (*1*–*4*). The coupling between one cavity photon and one elementary electronic excitation is quantified by the vacuum Rabi frequency, Ω. The nonperturbative strong light-matter coupling regime is achieved when Ω is larger than the loss rates of the photons and electronic excitations. Recently, growing interest has been generated by the ultrastrong coupling regime (*5*–*12*), which is obtained when the vacuum Rabi frequency becomes an appreciable fraction of the unperturbed frequency of the system, ω. In such a regime, it is possible to modify the ground- and excited-state properties obtaining nonadiabatic cavity QED effects (*5*). Experimental progress has been achieved in two different solid-state systems: (i) microcavities embedding doped quantum wells (*13*–*17*), where the active electronic transition is between quantized subbands in the well, and (ii) superconducting quantum circuits in transmission line resonators (*18*, *19*), where the photon field is coupled to artificial two-level atoms obtained with Josephson junctions.

We present experimental results on a high-mobility two-dimensional electron gas (2DEG) coupled to terahertz (THz) metamaterial resonators. The photon mode is coupled to the magnetic cyclotron transition of the 2DEG, obtained by applying a magnetic field perpendicular to the plane of the quantum wells (Fig. 1A). The cyclotron frequency is expressed by $\omega_c = \frac{eB}{m^*}$, where B is the applied magnetic field, e is the elementary charge, and m^* represents the electron effective mass. This highly controllable system is ideal for the study of strong coupling because the material excitation can be continuously tuned by changing the value of the applied magnetic field. The key physical aspect to

[1]Institute of Quantum Electronics, Eidgenössische Technische Hochschule Zürich, Switzerland. [2]Laboratoire Matériaux et Phénomènes Quantiques, Université Paris Diderot-Paris 7 and CNRS, Paris, France. [3]Laboratory for Solid State Physics, Eidgenössische Technische Hochschule Zürich, Switzerland. [4]Institut für Experimentelle und Angewandte Physik, Universität Regensburg, Germany.

*To whom correspondence should be addressed. E-mail: scalari@phys.ethz.ch

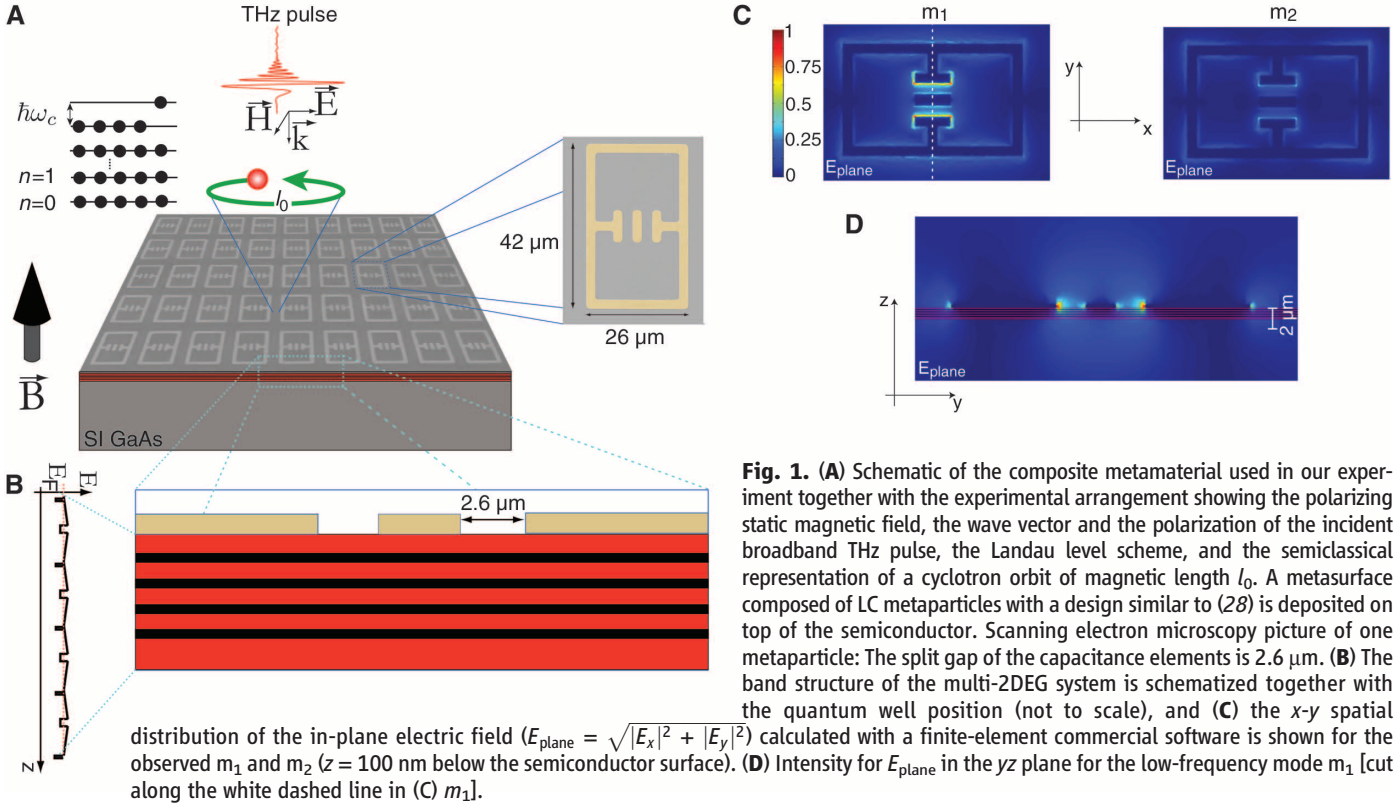

Fig. 1. (**A**) Schematic of the composite metamaterial used in our experiment together with the experimental arrangement showing the polarizing static magnetic field, the wave vector and the polarization of the incident broadband THz pulse, the Landau level scheme, and the semiclassical representation of a cyclotron orbit of magnetic length l_0. A metasurface composed of LC metaparticles with a design similar to (*28*) is deposited on top of the semiconductor. Scanning electron microscopy picture of one metaparticle: The split gap of the capacitance elements is 2.6 μm. (**B**) The band structure of the multi-2DEG system is schematized together with the quantum well position (not to scale), and (**C**) the *x*-*y* spatial distribution of the in-plane electric field ($E_{plane} = \sqrt{|E_x|^2 + |E_y|^2}$) calculated with a finite-element commercial software is shown for the observed m_1 and m_2 ($z = 100$ nm below the semiconductor surface). (**D**) Intensity for E_{plane} in the *yz* plane for the low-frequency mode m_1 [cut along the white dashed line in (C) m_1].

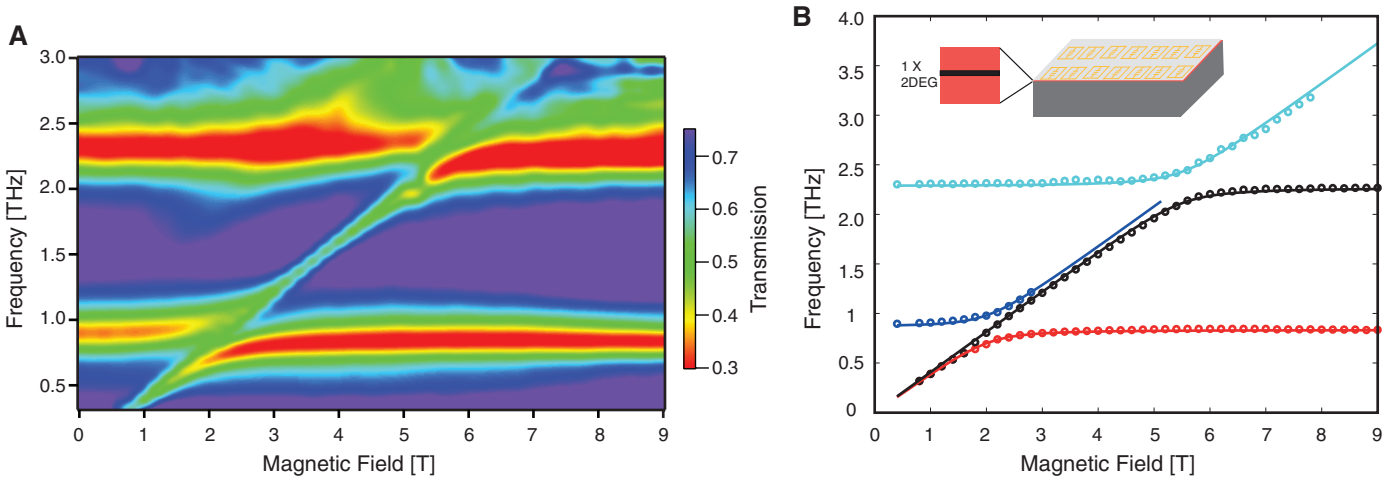

Fig. 2. (**A**) Transmission |t| of the sample (n_{QW} = 1) as a function of B. The reference is a plain 2DEG sample without resonators on top, and the measurement is performed at temperature (T) = 2.2 K. (**B**) Best fit with the extracted transmitted minima positions for the two different transverse modes of the electronic split-ring resonator; the fitting parameter is $\frac{\Omega}{\omega}$.

highlight is the dependence of the optical dipole moment, d, for a cyclotron transition on the cyclotron orbit length. The dipole d scales as $d \sim el_0\sqrt{\nu}$ (*20*), where $l_0 = \sqrt{\hbar/eB}$ is the magnetic length and $\nu = \rho_{2DEG}2\pi l_0^2$ is the filling factor of the 2DEG, with ρ_{2DEG} being the electron areal density. This proportionality of the dipole with respect to l_0 allows to have gigantic dipole moments as soon as the cyclotron transition can be resolved. According to theoretical calculations valid for integer filling factors and for an optimized resonator geometry, the coupling ratio is expected to scale as $\frac{\Omega}{\omega_c} \sim \sqrt{\alpha n_{QW}\nu}$, where α is the fine structure constant and n_{QW} is the number of 2DEGs (*20*). For high filling factors, this coupling ratio is predicted to assume values even larger than unity (corresponding to transitions in the microwave range). We used high-mobility 2DEG based on GaAs material system (*21*), and we realized our experiments in the THz region of the electromagnetic spectrum. These frequencies, for our material system, correspond to magnetic fields of the order of a few tesla, and optical experiments were conducted by using broadband THz pulses generated with ultrafast lasers (*22*). A THz–time domain spectroscopy (TDS) system (bandwidth 0.1 to 3 THz) (*23*) is coupled to a split-coil superconducting magnet to probe sample transmission (*24*).

Our THz metamaterial integrates the 2DEG with a metasurface of electronic split-ring resonators (Fig. 1A). These resonators (*25*–*28*) exhibit electric field enhancement over strongly subwavelength volumes (*29*), making them ideal candidates to reach extreme couplings in the mid-infrared and THz range, where long wavelength radiation has to interact with quantum well systems typically extending over lengths of some micrometers (*30*). Moreover, the enhanced in-plane (*x*-*y*) electric field couples efficiently to the cyclotron transition when the magnetic field is applied perpendicularly to the plane of the layers and parallel to the wave vector of the incident THz pulse (Fig. 1A). Resonators were deposited on top of the 2DEG by conventional photolitography, metallization with Ti/Au (5/250 nm), and lift-off technique.

At zero magnetic field, we observe two resonances, m_1 and m_2, whose origin is qualitatively different: the lowest frequency mode ($f_1 \approx$ 0.9 THz) is attributed to the LC resonance, where counterpropagating currents circulate in the inductive part and the electric field is enhanced mainly in the capacitor gap (*26*) (Fig. 1C). The second mode ($f_2 \approx 2.3$ THz) is attributed to the "cut wire" behavior, where a λ/2 kind of resonance is excited along the sides of the metaparticle (*27*). These values correspond well to simulations with 3D FE modeling (text S1). The two modes of the split-ring resonator also have different transverse wave vectors, as is evident looking at the different field distributions (Fig. 1C). The presence of conductive layers underneath alters the frequency and the quality factor of these resonances.

We observe a value of $Q_{1THz}^{(ins)} \simeq 4.3$ for an insulating substrate and $Q_{1THz}^{(2DEG)} \simeq 3.1$ when the resonator is deposited on top of the single 2DEG sample. The values for the second resonance results are less affected, yielding $Q_{2.3THz}^{(ins)} \simeq 5.3$ and $Q_{2.3THz}^{(2DEG)} \simeq 5.3$ (a more detailed analysis can be found in text S1). In contrast to atomic systems, we can realize strong light-matter coupling physics with resonators displaying extremely low quality factors. The giant value of the coupling constant $\Omega \sim \sqrt{n_{QW}\rho_{2DEG}}$ typical of intersubband systems (*5*) together with the high electric field enhancement of subwavelength metallic resonators ($V_{cav} \simeq 8 \times 10^{-17}$ m^3 in our case) allow the observation of cavity polaritons in a system where both components are in principle highly dissipative.

In the data reported in Fig. 2A, we observe the evolution of the sample transmission $|t| = \left|\frac{E_{Meta}(B)}{E_{2DEG}(0)}\right|$ as a function of the applied magnetic field (normalized to the electric field $E_{2DEG}(0)$ of the reference 2DEG wafer at B = 0 T). One 2DEG (n_{QW} = 1 and electron density $\rho_{2DEG}^{(1)} = 3.2 \times 10^{11}$ cm^{-2}) is used as an active medium and placed 100 nm below the surface: Its cyclotron resonance can couple to the resonator modes. As the magnetic field is swept, a profound modification of the sample transmission is observed. The possibility to tune in a continuous way the material excitation allows us to follow the evolution of polaritonic states as the system is driven from the uncoupled regime to the strongly coupled one (*31*). We observed two successive anticrossings when the cyclotron energy matches the first and the second resonator modes.

In Fig. 2B, we extracted the positions of the minima of sample transmission and plotted the dispersion curves for the polariton eigenvalues as a function of the magnetic field. The curves are calculated by using a full quantum mechanical treatment of the system, obtained generalizing the theory described in (*20*) to the case of a zero-dimensional resonator exhibiting two modes with different transverse wave vectors (*24*). Following a bosonization procedure, we have derived the different contributions to the total Hamiltonian and have diagonalized it by using the Hopfield-Bogoliubov method. The ideal resonator we have considered in the analytical treatment is different from the real split-ring one. However, we emphasize that this would introduce only a form factor in the matrix element calculation.

In order to fit the experimental data, we need to know the resonator modes frequencies (f_1' and f_2') as well as the strength of their couplings (Ω_1 and Ω_2). For each cavity mode, we assumed that the asymptotic value of the corresponding lower polariton branch coincides with the frequency of the unloaded resonator ($f_1' = 0.83$ THz and $f_2' = 2.26$ THz) (*20*, *24*). The coupling strength, $\frac{\Omega}{\omega}$, for the two modes

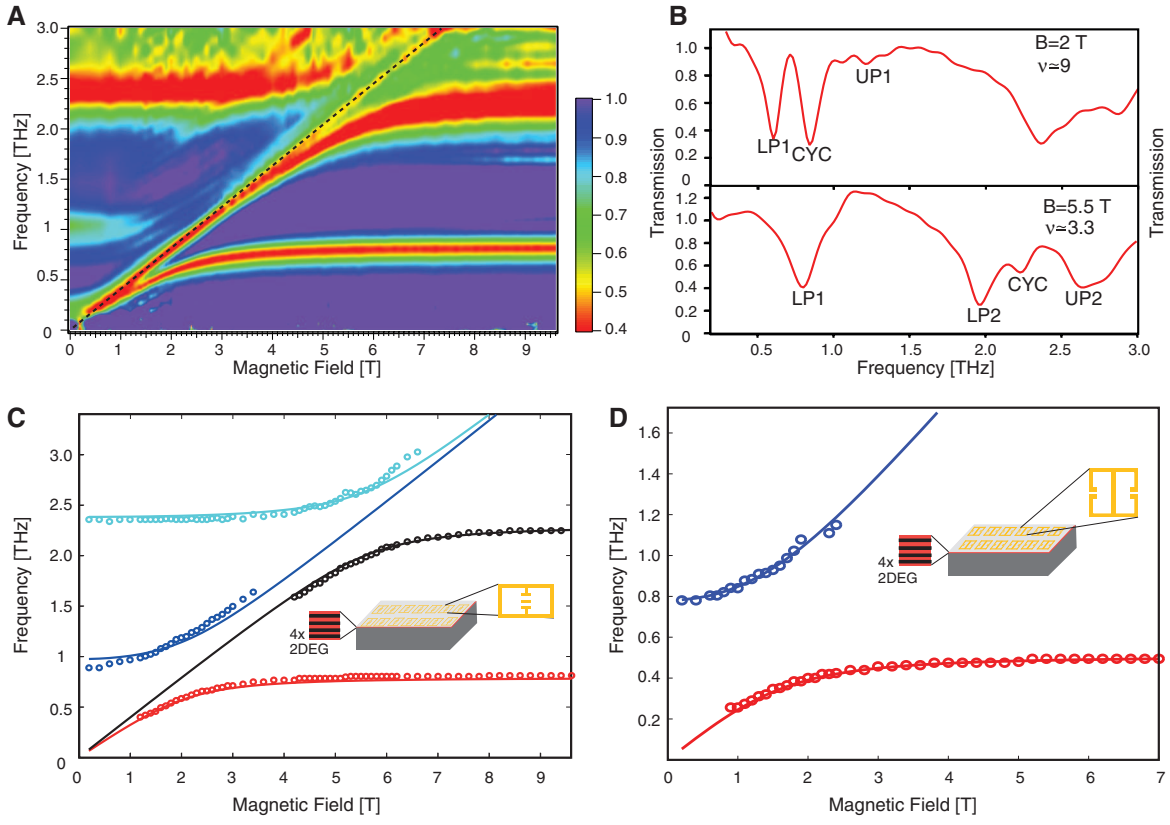

Fig. 3. (**A**) Transmission |t| of the sample ($n_{QW} = 4$) as a function of B. The reference is a plain 2DEG sample without resonators on top, and the measurement is performed at $T = 10$ K. The black dotted line highlights the cyclotron signal coming from the uncoupled material that is left between the resonators. (**B**) Sections in the two anticrossing regions for the sample transmission. (**C**) Best fit with the extracted transmitted minima positions for the two orthogonal modes of the split-ring electronic resonator; the fitting parameter is $\frac{\Omega}{\omega}$. (**D**) Best fit with the extracted transmitted minima positions for the $f = 500$ GHz resonator and $n_{QW} = 4$ measured at $T = 10$ K; the fitting parameter is $\frac{\Omega}{\omega}$. (Inset) Scheme of the 500-GHz resonator.

cannot be directly measured; we thus applied a best-fit procedure following the least square method, analogously to what done in (*14*) (more details in text S3). The minimal error (*24*) is obtained for $\frac{\Omega_1}{\omega_1} = 0.17$ and $\frac{\Omega_2}{\omega_2} = 0.075$ (where $\omega_1 = 2\pi f_1'$ and $\omega_2 = 2\pi f_2'$). As expected, the coupling strength scales monotonously with ν: for the measured density $\rho^{(1)}_{2DEG}$, we have $\nu(B) = \nu(2T) \simeq 6.5$ for the first mode and $\nu(B) = \nu(5.5T) \simeq 2.4$ for the second one.

To increase the coupling strength, we kept the resonator geometry, and hence the frequency constant, and increased the effective number of carriers in the system. A new sample was prepared with $n_{QW} = 4$ wells and an electron density per well of $\rho^{(4)}_{2DEG} = 4.45 \times 10^{11}$ cm^{-2} (Fig. 1B scheme and materials and methods). Sample transmission as a function of the applied magnetic field (Fig. 3A) shows that the system is driven deeply into the ultrastrong coupling regime. The polaritonic line widths display narrowing as the low quality cavity mode is mixed with the cyclotron resonance (Fig. 3B). Following the fitting procedure previously described, we observe a value of $\frac{\Omega_1}{\omega_1} = 0.36$ for the first resonance. Indeed, the effects of the antiresonant terms of the light-matter Hamiltonian start becoming relevant when the dimensionless ratio $\frac{\Omega}{\omega}$ is of the order of 0.1 (*14*). Because of the increased doping, the filling factor in the region of the anticrossing is $\nu \simeq 9$. As expected, the coupling ratio scales with $\sqrt{\rho_{2DEG} n_{QW}}$, and for the two samples at the same resonant frequency we obtain experimentally $\frac{\left(\frac{\Omega_1}{\omega_1}\right)_{n_{QW}=4}}{\left(\frac{\Omega_1}{\omega_1}\right)_{n_{QW}=1}} = \frac{0.36}{0.17} = 2.11$ and theoretically $\sqrt{\frac{4\rho^{(4)}_{2DEG}}{\rho^{(1)}_{2DEG}}} = 2.35$. The small discrepancy can be attributed to the different coupling of the quantum wells, which do not experience the same electric field of the resonator (Fig. 1D). The generalized expression of the coupling ratio is calculated in the case when all the wells are coupled in the same way to the resonator's field (*20*).

By further scaling the resonator frequency down to $f \simeq 500$ GHz with a slightly modified geometry (Fig. 3D inset, text S2, and fig. S5) and by using the sample with $n_{QW} = 4$ quantum wells, we could probe the regime where the polariton splitting at the anticrossing $2\hbar\Omega$ is larger than the bare cavity photon energy. In Fig. 3D, we report the positions of the minima of the sample transmission for the case of $f = 500$ GHz resonator together with the fitted dispersion curves. We measure a normalized ratio $\frac{\Omega_1}{\omega_1} = 0.58$ for a filling factor of $\nu(1.2T) \simeq 15.2$, which corresponds to $2\hbar\Omega \simeq 1.2\omega_c$ (fig. S6).

The generalization of the theory developed in (*20*) accounts for the depolarization shift in presence of a magnetic field (magnetoplasmon) originating from the long-wavelength part of the Coulomb interaction. We found that the renormalization of the cyclotron transition frequency is too small to allow the experimental resolution of the magnetoplasmon branch (Figs. 2A and 3A) in our experimental parameter regime, including the small wave vector condition $ql_0 << 1$, which is always satisfied because we are dealing with optical wave vectors.

We have observed ultrastrong light-matter coupling in a composite THz metamaterial measuring a normalized coupling ratio $\frac{\Omega}{\omega_c} = 0.58$. The impact of our results has to be considered also in the perspective of a change in the DC transport properties of the 2DEG, in analogy with what already observed by direct irradiation at lower frequencies (*31*).

These results should lead to the scaling of the frequency to lower values and to an increase of effective density to further enhance the coupling strength.

References and Notes

1. J. Raimond, M. Brune, S. Haroche, *Rev. Mod. Phys.* **73**, 565 (2001).
2. A. Wallraff *et al.*, *Nature* **431**, 162 (2004).
3. S. Christopoulos *et al.*, *Phys. Rev. Lett.* **98**, 126405 (2007).
4. K. Hennessy *et al.*, *Nature* **445**, 896 (2007).
5. C. Ciuti, G. Bastard, I. Carusotto, *Phys. Rev. B* **72**, 115303 (2005).
6. C. Ciuti, I. Carusotto, *Phys. Rev. A* **74**, 033811 (2006).
7. S. De Liberato, C. Ciuti, I. Carusotto, *Phys. Rev. Lett.* **98**, 103602 (2007).
8. M. H. Devoret, S. M. Girvin, R. J. Schoelkopf, *Ann. Phys. (Leipzig)* **16**, 767 (2007).
9. J. Bourassa *et al.*, *Phys. Rev. A* **80**, 032109 (2009).
10. V. M. Muravev, I. V. Andreev, I. V. Kukushkin, S. Schmult, W. Dietsche, *Phys. Rev. B* **83**, 075309 (2011).
11. T. Schwartz, J. A. Hutchison, C. Genet, T. W. Ebbesen, *Phys. Rev. Lett.* **106**, 196405 (2011).
12. P. Nataf, C. Ciuti, *Phys. Rev. Lett.* **104**, 023601 (2010).
13. D. Dini, R. Köhler, A. Tredicucci, G. Biasiol, L. Sorba, *Phys. Rev. Lett.* **90**, 116401 (2003).

14. A. Anappara *et al.*, *Phys. Rev. B* **79**, 201303 (2009).
15. G. Günter *et al.*, *Nature* **458**, 178 (2009).
16. Y. Todorov *et al.*, *Phys. Rev. Lett.* **105**, 196402 (2010).
17. M. Geiser *et al.*, *Phys. Rev. Lett.* **108**, 106402 (2012).
18. T. Niemczyk *et al.*, *Nat. Phys.* **6**, 772 (2010).
19. P. Forn-Díaz *et al.*, *Phys. Rev. Lett.* **105**, 237001 (2010).
20. D. Hagenmüller, S. De Liberato, C. Ciuti, *Phys. Rev. B* **81**, 235303 (2010).
21. V. Umansky *et al.*, *J. Cryst. Growth* **311**, 1658 (2009).
22. P. Smith, D. Auston, M. Nuss, *IEEE J. Quantum Electron.* **24**, 255 (1988).
23. D. Grischkowsky, S. Keiding, M. van Exter, C. Fattinger, *J. Opt. Soc. Am. B* **7**, 2006 (1990).
24. Supporting material is available on *Science* Online.
25. D. Schurig *et al.*, *Science* **314**, 977 (2006); 10.1126/science.1133628.
26. H.-T. Chen *et al.*, *Nature* **444**, 597 (2006).
27. W. J. Padilla, A. J. Taylor, C. Highstrete, M. Lee, R. D. Averitt, *Phys. Rev. Lett.* **96**, 107401 (2006).
28. J. O'Hara, E. Smirnova, A. Azad, H. Chen, A. J. Taylor, *Active Passive Electron. Components* **2007**, 10.1155/2007/49691 (2007).
29. C. Walther, G. Scalari, M. I. Amanti, M. Beck, J. Faist, *Science* **327**, 1495 (2010).
30. D. Shelton *et al.*, *ACS Nano Lett.* **11**, 2104 (2011).
31. The magnetic tunability has been studied in the very different system of exciton-polaritons in the near-infrared; see J. Tignon *et al.*, *Phys. Rev. Lett.* **74**, 3967 (1995).
32. R. G. Mani *et al.*, *Nature* **420**, 646 (2002).

Acknowledgments: This research was supported by the Swiss National Science Foundation (SNF) through the National Centre of Competence in Research Quantum Science and Technology and through SNF grant no. 129823. We thank J. Lloyd-Hughes and K. Ohtani for their help and S. S. Dhillon for discussions. C.C. is member of Institut Universitaire de France.

Supporting Online Material

www.sciencemag.org/cgi/content/full/335/6074/1323/DC1
Materials and Methods
SOM Text
Figs. S1 to S7
References (*33*, *34*)

31 October 2011; accepted 2 February 2012
10.1126/science.1216022

Laser Scribing of High-Performance and Flexible Graphene-Based Electrochemical Capacitors

Maher F. El-Kady,[1,2] Veronica Strong,[1] Sergey Dubin,[1] Richard B. Kaner[1,3]*

Although electrochemical capacitors (ECs), also known as supercapacitors or ultracapacitors, charge and discharge faster than batteries, they are still limited by low energy densities and slow rate capabilities. We used a standard LightScribe DVD optical drive to do the direct laser reduction of graphite oxide films to graphene. The produced films are mechanically robust, show high electrical conductivity (1738 siemens per meter) and specific surface area (1520 square meters per gram), and can thus be used directly as EC electrodes without the need for binders or current collectors, as is the case for conventional ECs. Devices made with these electrodes exhibit ultrahigh energy density values in different electrolytes while maintaining the high power density and excellent cycle stability of ECs. Moreover, these ECs maintain excellent electrochemical attributes under high mechanical stress and thus hold promise for high-power, flexible electronics.

Batteries and electrochemical capacitors (ECs) stand at opposite ends of the spectrum in terms of their power and energy densities (*1*). Batteries store energy through electrochemical reactions and can exhibit high energy densities (on the order of 20 to 150 Wh/kg), whereas ECs, which store charge in electrochemical double layers (EDLs), can only achieve values of 4 to 5 Wh/kg (*2*–*4*). However, because ion flow is faster than redox reactions ECs can deliver much higher power densities. ECs are also generally maintenance free and display a longer shelf and cycle life, so they are often favored in many electronic applications (*2*–*4*).

An EC that combines the power performance of capacitors with the high energy density of batteries would represent a major advance in energy storage technology (*5*, *6*), but this requires an electrode with higher and more accessible surface area than that of conventional EC electrodes while maintaining high conductivity. Graphene-based materials are attractive in this regard because of their mechanical and electrical properties as well as exceptionally high surface area. Recently, the intrinsic capacitance of single-layer graphene was reported to be ~21 μF/cm^2; this value now sets the upper limit for EDL capacitance for all carbon-based materials (*7*). Thus, ECs based on graphene materials could, in principle, achieve an EDL capacitance as high as ~550 F/g if their entire surface area could be used.

Currently, graphene-based materials derived from graphite oxide (GO) can be manufactured on the ton scale at low cost, making them potentially cost-effective materials for charge storage devices (*8*). Although these graphene-based materials have shown excellent power density and life-cycle stability, their specific capacitance (130 F/g in aqueous potassium hydroxide and 99 F/g in an organic electrolyte) still falls far below the theoretical value of 550 F/g calculated for single-layer graphene (*9*). A variety of other graphene-based materials derived from GO have also been used, yet the values of specific capacitance, energy density, and power density have remained lower than expected (*10*–*13*)—an effect often attributed to the restacking of graphene sheets during its processing as a result of the strong sheet-to-sheet van der Waals interactions. This reduction in the specific surface area of graphene accounts for the overall low capacitance. In addition, these ECs exhibited relatively low charge/discharge rates, which precludes their use for high-power applications. Recently, EC devices composed of curved graphene (*14*), activated graphene (*15*), and solvated graphene (*16*) have demonstrated enhanced performance in terms of energy density. However, further improvements in energy density are needed that do not sacrifice high power density. In particular, the

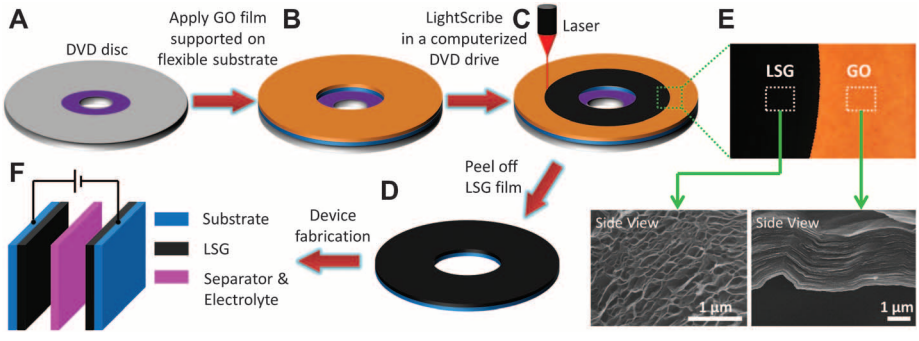

Fig. 1. Schematic illustration of the fabrication of laser-scribed graphene-based electrochemical capacitors. (**A** to **D**) A GO film supported on a flexible substrate is placed on top of a LightScribe-enabled DVD media disc, and a computer image is then laser-irradiated on the GO film in a computerized LightScribe DVD drive. (**E**) As shown in the photograph, the GO film changes from golden brown color to black as it reduced to laser-scribed graphene. The low-power infrared laser changes the stacked GO sheets immediately into well-exfoliated few-layered LSG film, as shown in the cross-sectional SEM images. (**F**) A symmetric EC is constructed from two identical LSG electrodes, ion-porous separator, and electrolyte.

[1]Department of Chemistry and Biochemistry and California NanoSystems Institute, University of California, Los Angeles (UCLA), Los Angeles, CA 90095, USA. [2]Department of Chemistry, Faculty of Science, Cairo University, Giza 12613, Egypt. [3]Department of Materials Science and Engineering, UCLA, Los Angeles, CA 90095, USA.

*To whom correspondence should be sent. E-mail: kaner@chem.ucla.edu